



Integration of piezo-based active shape control into composite engine fan blades for future electrified aircraft

Felix Kleinwechter^{1,4} · Ahmad Naderi^{2,4} · Abbas Mehraban^{2,4} · Thomas Ruminy^{3,4} · Marcel Seidler^{3,4} · Hans Peter Monner^{1,4} · Michael Terörde^{2,4} · Jens Friedrichs^{3,4}

Received: 14 March 2025 / Revised: 4 July 2025 / Accepted: 21 October 2025
© The Author(s) 2026

Abstract

The blades of modern aero-engines are conceived for a specific design point. Due to the resulting fixed geometry of the blade, maximum engine efficiency can be achieved only for design point conditions. In order to improve the efficiency during off-design operation, applying blades with active shape control can be beneficial. Therefore, morphing fan blades, which adapt their geometry to the prevailing conditions by using piezoelectric low-profile actuators, are researched. Prior to the construction of a morphing fan blade demonstrator, a sequential multidisciplinary analysis is required to assess the feasibility of piezoelectric actuation in fan blades of future aircraft. First, the aerodynamic geometry of the fan blade is designed with respect to maximising the deformability. Subsequently, the structure of the morphing blade is developed, including a drapability analysis of the actuators and a numerical simulation of the achievable morphing deformation. Finally, the developed morphing structure is employed to examine a sufficient electrical power supply system for the morphing technology in a future electrified aircraft.

Keywords Morphing · CFRP · Turbofan · Electric Propulsion

Abbreviations

<i>AC</i>	Alternating Current	<i>EPS</i>	Electric Power System
<i>ACP</i>	Ansys Composite PrepPost	<i>FEA</i>	Finite Element Analysis
<i>CFRP</i>	Carbon Fiber Reinforced Polymer	<i>HVA</i>	High Voltage power Amplifier
<i>DC</i>	Direct Current	<i>I²C</i>	Inter-Integrated Circuit
<i>EES</i>	Electromechanical Energy Storage	<i>LE</i>	Leading Edge
		<i>MFC</i>	Macro Fiber Composite

These authors contributed equally to this work.

✉ Felix Kleinwechter
felix.kleinwechter@dlr.de

Ahmad Naderi
ahmad.naderi@tu-braunschweig.de

Abbas Mehraban
abbas.mehraban@tu-braunschweig.de

Thomas Ruminy
thomas.ruminy@tu-braunschweig.de

Marcel Seidler
marcel.seidler@tu-braunschweig.de

Hans Peter Monner
hans.monner@dlr.de

Michael Terörde
michael.teroerde@tu-braunschweig.de

Jens Friedrichs
jens.friedrichs@tu-braunschweig.de

¹ Institute of Lightweight Systems, German Aerospace Center (DLR), Lilienthalplatz 7, 38108 Braunschweig, Lower Saxony, Germany

² Institute for Electromagnetic Compatibility, Technical University Braunschweig, Schleinitzstraße 23, 38106 Braunschweig, Lower Saxony, Germany

³ Institute of Jet Propulsion and Turbomachinery, Technical University Braunschweig, Hermann-Blenk-Straße 37, 38108 Braunschweig, Lower Saxony, Germany

⁴ Cluster of Excellence SE²A - Sustainable and Energy Efficient Aviation, Braunschweig, Germany

<i>MPC</i>	Multi Point Constraint	<i>G</i>	shear modulus
<i>PS</i>	Pressure Side	<i>l</i>	length
<i>PTF</i>	Propulsion Testing Facility	<i>M</i>	mass
<i>PWM</i>	Pulse Width Modulation	<i>Ma</i>	Mach number
<i>PZT</i>	Lead Zirconate Titanate	\dot{m}	mass flow rate
<i>SE²A</i>	Sustainable and Energy Efficient Aviation	<i>N</i>	number
<i>SMA</i>	Shape Memory Alloys	<i>P</i>	power
<i>SS</i>	Suction Side	<i>s</i>	spanwise position
<i>TE</i>	Trailing Edge	<i>T</i>	time
<i>TOC</i>	Top Of Climb	<i>Th</i>	thrust
<i>UHBR</i>	Ultra High Bypass Ratio	<i>Tr</i>	throttle
<i>VHBR</i>	Very High Bypass Ratio	<i>U</i>	voltage
Indices		U_{Cell}	total strain energy
<i>act</i>	actuator	U_{N}	normal strain energy
<i>e</i>	end	U_{RMS}	effective voltage
<i>el</i>	electric	U_{S}	shear strain energy
<i>HVA</i>	high voltage power amplifier	<i>v</i>	velocity
<i>is</i>	isentropic	<i>V</i>	volume
<i>M</i>	morphing	<i>X</i>	cartesian coordinate
<i>max</i>	maximum	<i>XC</i>	impedance of capacitive load
<i>MFC</i>	MFC actuator	<i>Y</i>	cartesian coordinate
<i>n</i>	negative	<i>Z</i>	cartesian coordinate
<i>p</i>	positive	α	net fiber angle
<i>pr</i>	propulsion	β	actuator angle relative to X-Y plane
<i>ref</i>	non-deformed	γ	shear angle
<i>s</i>	start	γ_{Lock}	locking angle
<i>shaft</i>	engine shaft	$\Delta\varphi$	turning angle
<i>tot</i>	total	ϵ	normal shear strain
<i>wrinkle</i>	position of wrinkling	ζ	shear strain
\parallel	fiber direction	Θ	fiber orientation angle
\perp	transverse direction	η	efficiency
<i>1nF</i>	capacitance of 1 nF	ν_{ht}	hub-to-tip-ratio
		ω	unidirectional weighting factor

Variables

<i>A</i>	area
<i>AR</i>	aspect ratio
<i>c</i>	chordwise position
<i>C</i>	capacitance
<i>D</i>	deformation
<i>E</i>	Young's modulus
<i>f</i>	frequency

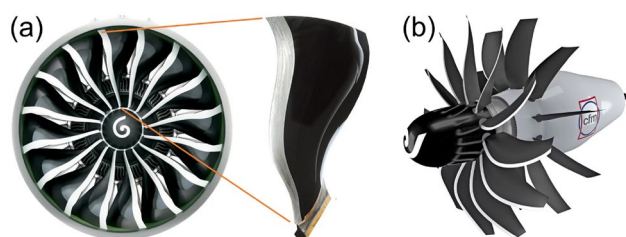


Fig. 1 Engines with CFRP blades: **a** General Electric GE9X VHBR engine [4], **b** cfm RISE open rotor engine [5]

1 Introduction and motivation

A key factor in the high efficiency of modern turbofan engines is the continuous increase in bypass ratio to Very High Bypass Ratio (VHBR) engines, which is enabled by state-of-the-art fan section designs [1]. In order to achieve the resulting high performance specifications, lightweight fan blade designs are necessary. Development with conventional titanium alloys is well advanced and offers little scope for further performance improvements [2]. Consequently, the GE 90 engine was the first to utilize fan blades made of Carbon Fiber-Reinforced Polymers (CFRP), which open up new possibilities with their orthotropic material properties and high specific strength [3]. Figure 1 (a) shows an example of a VHBR engine with CFRP fan blades.

Future electric and hybrid engine architecture concepts using batteries, fuel cells or sustainable aviation fuels, as

well as more efficient propulsion architectures such as open rotor configurations (Fig. 1 (b)), will also utilize blade-based propulsion [6]. Increasing propulsive efficiency of the blading will therefore continue to be of great importance for achieving ambitious environmental goals in the future. The geometries of current blading systems are conceived for a design point, which is usually characterized by the most critical condition in the form of Top-Of-Climb (TOC) [7]. Due to the fixed geometry of blades, maximum efficiency is only achieved at the design point. To avoid a decrease in efficiency during off-design phases such as cruise, landing and take-off, this research proposes shape-adaptive rotor blading. The necessity for shape-variable fan blading is augmented by further off-design operating scenarios, such as crosswind events or the ingestion of the fuselage boundary layer. Both operating scenarios lead to inlet distortion and therefore a locally increased flow incidence and reduced propulsive efficiencies [8].

Shape-variable engine blades, which can provide improved geometries for different flight phases and conditions through morphing, have not yet been utilized in the aviation industry and only limited scientific research has been conducted. However, pitch-variable guide vanes are used in aero engines, which modify the stagger angle by turning the entire non-rotating stator blades around the radial direction with lever mechanisms [9]. The adaptation of this pitch adjustment technology to rotating blades such as fan blades is challenging due to high centrifugal loads during operation, and is therefore subject to current research [10–12]. In contrast to a shape-morphing approach, the pitch adjustment allows only for a constant spanwise stagger angle modification, but not for local adjustment of the geometry (e.g. at tip). Furthermore, it is impossible to modify the profile cambering or a simultaneous adaptation of both, staggering and cambering.

The development of shape-adaptive rotors has been successfully achieved outside of engine blades. Van der Wall et al. and Kalow et al. [13, 14] developed helicopter rotor blades that allow for active adaptation of the blade's twist by integrated piezoelectric actuators. Fortini et al. and Suman et al. [15, 16] tested morphing heavy-duty automotive cooling

axial fan blades. The shape adaptation is controlled by the temperature of the air flow using Shape Memory Alloy (SMA) actuators embedded into the fiberglass reinforced polymer structure of the blade. However, research on morphing aero engine blading is mostly limited to non-rotating shape-adaptive compressor cascades. Krone et al. [17] show experimentally that the turning angle of the cascade's profiles can be adjusted by $\pm 1^\circ$ using applied piezoelectric actuators, while Li et al. [18] were able to demonstrate an increase in efficiency of 80 % in a supersonic cascade under low-upstream-mach-number conditions using comparable actuation. Abate et al. [19] use integrated actuators made of SMA to adapt the leading edge of the profiles in the cascade to different inflow conditions.

The potential of rotating morphing engine blades is demonstrated by Tweedt [20]. In aerodynamic simulations, the fan blade morphing results in an increase in aerodynamic performance, but the structural realization of the analyzed shape change is not considered. In addition, morphing technology for aero engine rotor blades is developed as part of the Sustainable and Energy Efficient Aviation (SE²A) Cluster of Excellence. Montano et al. [21–23] developed a multidisciplinary design methodology for morphing metallic compressor blades through the utilization of low-profile piezoelectric actuators. Numerical simulations show an achievable change in profile cambering of approximately 1° . Kleinwechter et al. [24] extended the methodology to enable the design of morphing fan blades made of CFRP with the objective to manufacture and test scaled morphing VHBR fan blade demonstrators. By tailoring the laminate structure, the weight of the blade architecture could be reduced by 66.2 % and the achievable morphing deformation could be increased by up to 97.2 % compared to titanium alloy blade bodies [24].

The scope of this paper are preliminary investigations to confirm the feasibility of the morphing concept for the intended manufacturing and experimental investigation of morphing CFRP fan blades. Therefore, the morphing fan technology is analyzed sequentially (Fig. 2), starting from the blade's aerodynamic geometry to the blade's structure including the drapability of piezoelectric actuators and calculation of morphing deformation to the integration of the developed morphing fan technology into future electrified aircraft.

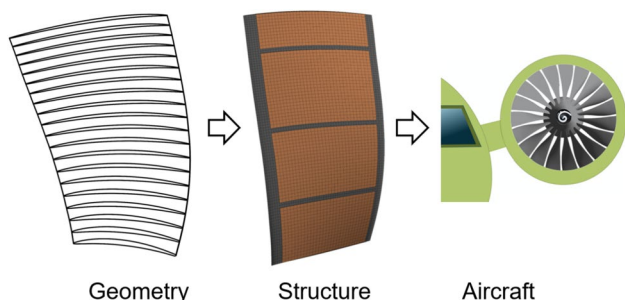


Fig. 2 Sequential structure of feasibility analysis.

2 Fan blade geometry

The double-curved topology of the fan blade is derived following the aerodynamic design procedure summarized in [25]. Originally, the turbofan was designed for test rig application at ground level conditions. Due to the test rig

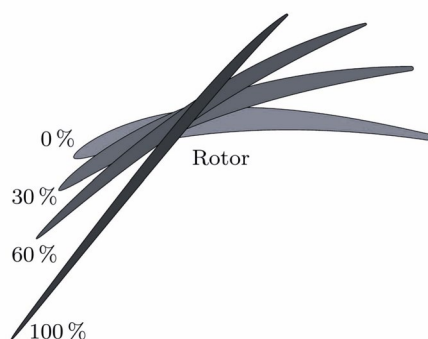


Fig. 3 Fan profile sections at different blade heights with 0% equal to root

dimensions, the fan geometry is a scaled version of current low hub-to-tip ratio Ultra High Bypass Ratio (UHBR) fan designs and follows corresponding design specifications. The fan stage is designed for a pressure ratio of 1.37 and a mass flow \dot{m} of 63.33 kg s^{-1} . The chosen on-design operating point has a maximum power limitation of 2.0 MW, which together with an isentropic efficiency of $\eta_{is} = 0.92$ defines its maximum achievable propulsive power of 1.82 MW. In addition to a low hub-to-tip ratio of $\nu_{ht} = 0.26$, an aspect ratio of $AR = 1.95$ results in a slender blade shape. While the hub-to-tip ratio results from current UHBR fan design trends, the high aspect ratio was chosen to boost the fan rotor's deformability towards a piezoelectric actuation. For a similar reason, the fan rotor exhibits a forward swept blade, which is determined by a hub sweep angle of 10° . The modeling of the blade profiles follows an extended Class-Shape-Function Methodology [25], while the respective profile prototypes along the blade span are selected based on the corresponding relative inflow Mach number (Fig. 3).

The maximum Mach number of $Ma = 1.15$ at the blade tip determines a transonic wedge shaped blade profile design, while profiles with increased leading edge thickness are used near the hub to allow for a higher flow incidence tolerance, as no piezoelectric morphing can be achieved here, as shown by [23].

3 Piezoelectric actuation for double-curved blade structure

The following section aims to investigate the drapability of piezoelectric low-profile actuators on the double-curved Pressure and Suction Side (PS and SS) of the blade developed in sect. 2 and to quantify the achievable morphing deformation of the structure. First, the structure of the piezoelectric actuators used is described. Next, the methodology is presented, which includes the simulation of the draping behavior with a pin-jointed-net model, the experimental

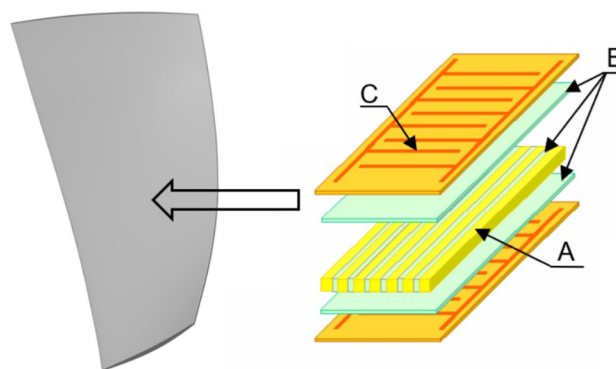


Fig. 4 Structure of the MFC actuator [27] to be draped onto the fan geometry from SE²A

determination of a draping limit value, and the simulative prediction of the morphing deformation with a Finite Element Analysis (FEA).

Based on the simulated draping behavior and the limit value, the PS and SS actuators are divided into multiple individual actuators to enable the draping. After an experimental confirmation of the drapability prediction, the influence of the necessary actuator splitting is analysed. Therefore, the achievable morphing deformation of the developed divided actuator set-up under operational centrifugal loads is simulated and compared with the continuous, non-divided actuator setup. Finally, the expected aerodynamic effects are discussed.

3.1 Piezoelectric low-profile actuators

Compact low-profile piezoelectric actuators utilize the inverse piezoelectric effect, which converts electrical energy into precise mechanical movements [26]. For this investigation, the P1 type Macro Fiber Composite (MFC) actuator, produced by Smart Materials Corp. [27], is chosen. Figure 4 depicts the structure of these MFC actuators and the geometry of the scaled SE²A fan blade from sect. 2.

The MFCs consist of piezoceramic rectangular fibers (A in Fig. 4) made of lead zirconate titanate (PZT), which are embedded in an epoxy resin matrix and have an epoxy resin cover layer on top and bottom (B in Fig. 4). This composite is located between two polyimide films into which interdigital electrodes are integrated (C in Fig. 4). This design offers flexibility, durability, and high performance, making MFCs suitable for applications in aerospace, robotics, and smart structures. An application of a voltage to the electrodes generates an electric field that acts on the piezoelectric fibers, leading to strain caused by the inverse piezoelectric effect [26].

The chosen P1 type MFC uses the d_{33} operation mode of piezoelectric actuation, where the electric field and piezoelectric strain are aligned along the same axis,

which maximizes the achievable actuation. At a voltage of 1500 V, MFCs exhibit a maximum possible expansion, while at -500 V a maximum possible contraction [27].

3.2 Methodology

As the area of the low-profile actuators increases, the drapability on the double-curved surfaces of the blade becomes increasingly limited, so that a subdivision into individual smaller actuators may become necessary. The simulation methodology must therefore ensure drapability by splitting the actuators and consider the effects of the splitting on the morphing performance.

3.2.1 Draping methodology

In the production of layered composite structures, reinforced plies such as CFRP prepregs are positioned with an intended fiber orientation onto a mold surface. If the molding surface exhibits a double curvature, the plies can only adapt by in-plane deformation during draping. The drapability of materials depends on the dominant draping mechanism, which can be in-plane elongation and compression or in-plane shear. The analysis of draping effects is pertinent for two reasons. First, in-plane shear changes the intended fiber orientation, which must be considered in the design process. Second, for the assessment of manufacturability, since exceeding the drapability limits of elongation/contraction and shear leads to wrinkling. The widely used methods for draping simulation are developed for fabrics (especially woven fabrics) and are mainly utilized in the design of double-curved fiber composite structures. Methods for the simulation of draping and wrinkling for other materials such as polyimide film from the MFCs do not exist so far [28].

The objective of this study is not to develop a novel draping methodology. Instead, the usability of a commercially available algorithm for the specific fan blade-actuator problem will be analyzed and tested. Since the CFRP blade laminate and the MFC actuators are modeled in the FEA using Ansys Composite PrepPost (ACP) as shown in [24], the ACP internal draping algorithm [29] can be utilized. This

algorithm does not only allow for the simulation of woven fabrics but also allows to consider unidirectional fabrics. For woven fabrics, the shear stiffness is negligible up to a certain deformation, so that draping can be modeled by pure in-plane shear. In unidirectional mode, the algorithm also allows the consideration of in-plane elongation/contraction in transverse direction, while fibers are idealized as inextensible.

Therefore, the MFC actuator is idealized as a unidirectional fabric with ideally rigid PZT fibers. The draping simulation methodology for unidirectional prepregs is based on a modified approach for woven fabric products. A pin-jointed-net model according to Wang et al. [30] is employed. Plies are idealized via a net of draping cells, as illustrated in Fig. 5.

The draping cells are composed of net fibers that are interconnected by nodes (pins). During the draping process, the net fibers are capable of rotating freely around the pins and transverse net fibers (Y-direction) can undergo strain. Longitudinal net fibers (X-direction), which define the direction of the PZT fibers in the actuator, are inextensible.

During the draping simulation, the draping cells are successively applied to the double-curved surface starting from a seed point. The necessary in-plane deformation by elongation/contraction and shear is calculated using a strain energy minimization approach. Normal strain energy U_N is described by:

$$U_N = \frac{1}{2} V E \epsilon^2 \quad (1)$$

With the Young's modulus E , the volume V and the normal shear strain ϵ , which is defined by the original length of the transverse draping cell edge l_{ref} and the elongated length l :

$$\epsilon = \frac{l - l_{ref}}{l_{ref}} \quad (2)$$

The shear strain energy U_S is described by:

$$U_S = \frac{1}{2} G \zeta^2 \quad (3)$$

With the elastic shear modulus G and the shear strain ζ , which can be approximated by the angle between the originally orthogonal net fibers α :

$$\zeta = \cos \alpha \quad (4)$$

The total shear strain energy U'_S for a given draping cell is defined by the sum in all four corners:

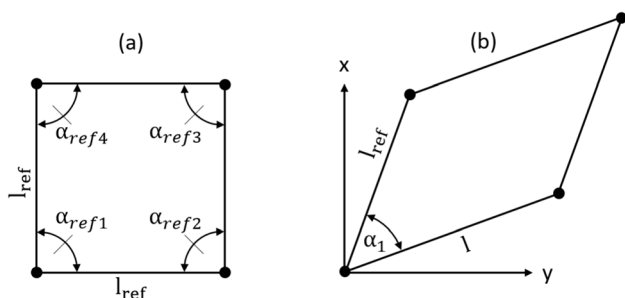


Fig. 5 Draping cell: **a** Undeformed, **b** Deformed

$$U'_S = \sum_{i=1}^4 \frac{1}{2} G \cos^2 \alpha_i \tag{5}$$

Therefore, the combined normal and shear strain energy in a draping cell U_{Cell} is given by:

$$U_{Cell} = \sum_{i=1}^4 \frac{1}{2} G \cos^2 \alpha_i + \frac{1}{2} VE \frac{(l - l_{ref})^2}{(l_{ref})^2} \tag{6}$$

The constants can be excluded for the energy minimization problem. With a unidirectional weighting factor $\omega \in [0, 1]$, the minimization problem becomes:

$$\min U_{Cell} = (1 - \omega) \sum_{i=1}^4 \cos^2 \alpha_i + \omega \frac{(l - l_{ref})^2}{(l_{ref})^2} \tag{7}$$

The weighting factor is a central component of Ansys ACP’s unidirectional draping methodology. It controls the amount of elongation deformation. When ω is set to zero, only shear deformation is considered and the unidirectional draping approach is reduced to a woven model. A unidirectional weighting factor of $\omega = 0.2$ is used for the MFC actuator. The reason for this is that the polyimide of the actuators provides good shearability with moderate elongation/contraction [31]. The simulation output is the shear angle of the draping cells, which is highest in areas of strong double curvature. Based on these results, the deviation of the predicted fiber orientation is calculated.

3.2.2 Experimental determination of locking angle

To ensure the applicability of the actuators, it is necessary that the resulting shear angle does not exceed a specific limit value, referred to as locking angle. It is not possible to apply the experimental methods used to determine the shearability of textiles like woven CFRP fabrics to film-like materials due to the higher shear stiffness of the latter [28]. Sanack et al. [32] investigated the shearability of auxiliary film-like materials for vacuum bagging of CFRP parts. The established frame test method for determining the shearability was inapplicable in those cases due to the materials’ much smaller locking angle. The MFC actuators with their polyimide films present similar challenges. As the objective of this study is not to develop a universally applicable draping methodology for non-textile layers, the locking angle of the fan blade is determined through experimental application on a 3D-printed blade model. Consequently, the results are limited to the specific blade-actuator problem and cannot be generalized.

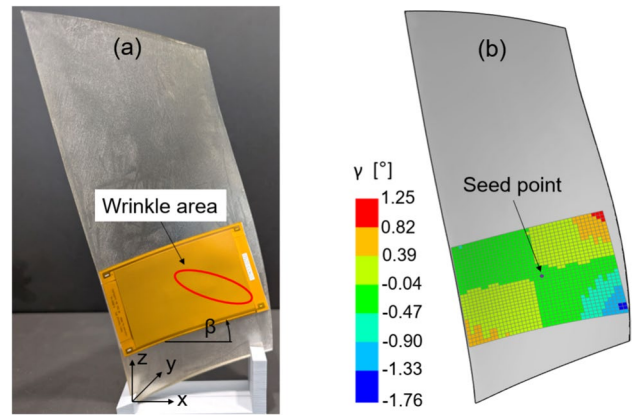


Fig. 6 Experimental draping analysis: a Actuator position with start of wrinkling, b Simulated corresponding shear angles.

Table 1 Position of actuator with wrinkling.

$X_{wrinkle}$	$Y_{wrinkle}$	$Z_{wrinkle}$	$\beta_{wrinkle}$
1 mm	5.03 mm	37 mm	9.5°

The applicability of the actuators is analyzed using an M-8557-P1 actuator with a total length of 103 mm and a total width of 64 mm. The double curvature of the blade is least pronounced at the tip and increases in the direction of the root. Hence, moving the actuator towards the blade root may provoke wrinkling effects. Figure 6 (a) shows the actuator position from which application was no longer possible due to the occurrence of wrinkling. The onset of wrinkling is noticeable during application, but can not be seen in Fig. 6.

The position of the actuator on the blade where wrinkling occurs is described by the Cartesian coordinates $X_{wrinkle}$, $Y_{wrinkle}$, and $Z_{wrinkle}$ of the lower left corner of the actuator and the angle relative to the X-Y plane $\beta_{wrinkle}$. Tab. 1 displays the wrinkle position of the MFC.

Figure 6 (b) shows the corresponding draping simulation of the actuator following the methodology described in Sect. 3.2.1. The center of the actuator is defined as the seed point for the draping simulation, as this location exhibits the most even compensation for double curvature and produces the lowest fiber deviation. The simulation provides an absolute locking angle of $\gamma_{Lock} = 1.76^\circ$ as a result.

3.2.3 Morphing calculation methodology

The calculation of the morphing deformation under the centrifugal loads occurring during operation is automated with the methodology proposed by Kleinwechter et al. [24] using modules from Ansys Workbench. First, surface models of the blade’s pressure and suction side are generated based on the profiles of the blade from sect. 2 as shown in Fig. 7 (a). Actuator shapes are then defined relative to the dimensions of the PS and SS by specifying their extension in chord- and spanwise direction, resulting in surface

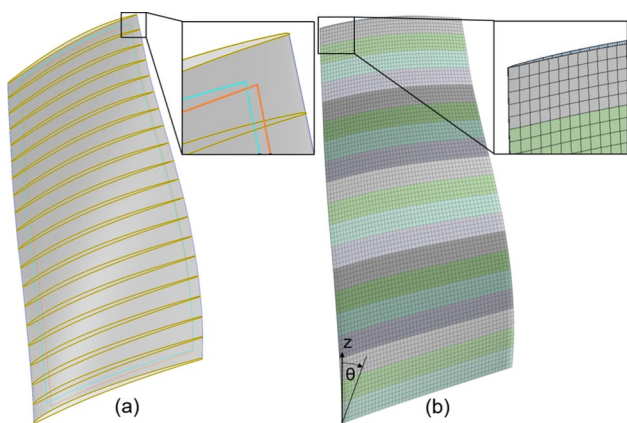


Fig. 7 Blade modeling: **a** PS and SS with profile sections in yellow and limiting lines of actuators in orange for PS and turquoise for SS, **b** Meshed PS and SS surfaces

models of the actuators. The blade and actuator surfaces are homogeneously meshed using quadratic shell elements with 4 nodes per element (SHELL181). Figure 7 (b) illustrates the meshed SS and PS of the blade. Based on the meshed surfaces, the CFRP laminate structure of the blade body and the structure of the actuators are defined using ACP.

The blade’s CFRP laminate is modeled by draping 42 individual shaped plies of the unidirectional prepreg Hex-Ply M21E from Hexcel Corp. into the blade body. Based on the resulting definition of the laminate with shell elements, the shell elements are transformed into solid elements with 8 nodes per element (SOLID185). The desired fiber orientations of the plies are defined using the orientation angle

θ (Fig. 7). An orientation angle of $\theta = 0^\circ$ represents the radial direction.

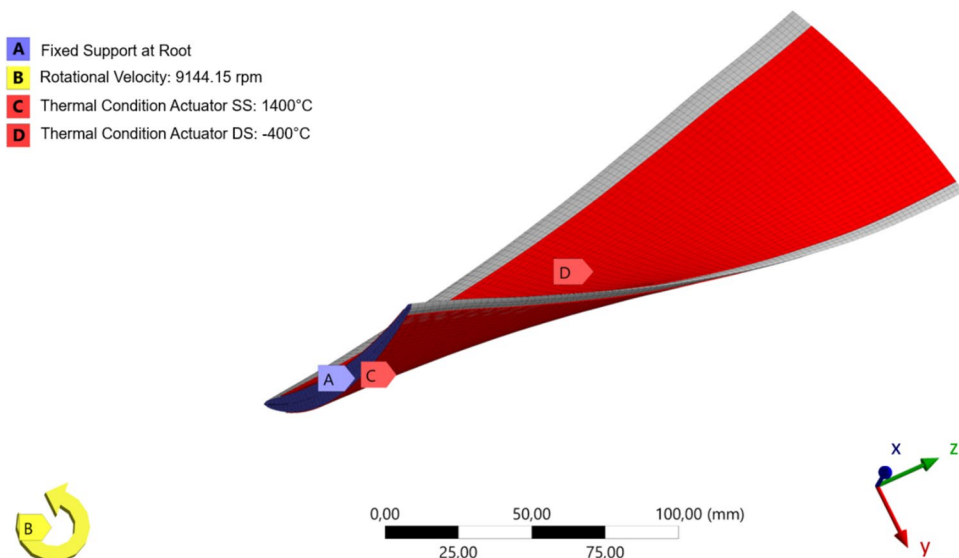
Following the research of Williams [33], the entire MFC structure is modeled as an orthotropic unidirectional thin material on the basis of classical laminate theory. In the FEA, the piezoelectric actuation of the MFCs is simulated in a simplified approach using a thermal analogy. The thermal expansion coefficients in the MFC material model are therefore defined in a manner that the thermal induced strain at a temperature increase of 1°C corresponds to the piezoelectric strain under an applied voltage increase of 1 V. This results in maximum expansion of the actuators at 1500°C (representing 1500 V) and maximum contraction at -500°C (representing -500 V). However, based on the findings of Monner et al. [34], the actuators are only operated at -400 V to 1400 V to avoid damage, which defines the temperature between -400°C and 1400°C . Tab. 2 shows the orthotropic material constants describing the linear elastic material behavior as well as the thermal expansion coefficients for the thermal analogy. The index \parallel describes properties in fiber direction, while \perp transverse properties.

Once the structural models of the blade body and the actuators are available, they are connected by a bonded contact approach using Multi Point Constraint (MPC) formulations. Figure 8 visualizes the final structural model as well as the boundary conditions and loads applied. Given that only the aerodynamic blade body is present without the blade mount, the connection of the blade to an engine disk is

Table 2 MFC: Orthotropic elastic constants and expansion coefficients for thermal analogy

Young’s modulus [GPa]		Poisson’s ratio [-]		Shear modulus [GPa]		Thermal exp. coef. [K^{-1}]	
E_{\parallel}	30	$\nu_{\perp\parallel}$	0.35	$G_{\perp\parallel}$	10.7	a_{\parallel}	$8.3 \cdot 10^{-7}$
E_{\perp}	15.5	$\nu_{\perp\perp}$	0.4	$G_{\perp\perp}$	5.7	a_{\perp}	$3.96 \cdot 10^{-7}$

Fig. 8 Structural model of morphing fan blade with boundary condition and loads



idealized by defining the blade's root profile as a fixed support. To calculate the morphing deformation under centrifugal loads, two load steps are carried out in the FEA, taking large deformations into account.

In the first step, the deformation \underline{D}_1 of the blade is calculated at a rotation of 9144.15 rpm, for which the fan was designed. In the second step, in addition to rotation, the actuators are activated by defining thermal boundary conditions in the actuators, resulting in the deformation \underline{D}_2 that combines centrifugal loads and morphing. The morphing deformation \underline{D}_M alone results in:

$$\underline{D}_M = \underline{D}_2 - \underline{D}_1 \quad (8)$$

With the deformation defined by the directional displacements of the mesh nodes in X , Y and Z direction:

$$\underline{D} = (D_X \ D_Y \ D_Z) \quad (9)$$

The morphing deformation is transferred to an evaluation tool following Seidler et al. [23]. This tool re-engineers the camber lines of the deformed profile sections. In this way, the morphing-related change in profile angles, such as the turning angle $\Delta\varphi$, can be calculated.

3.3 Results of draping analysis

To analyze the applicability of the actuators and the effect on the morphing performance, a blade configuration must first be defined. To simplify the analysis and focus on the actuators, all CFRP fibers within the blade body have been oriented at $\theta = 0^\circ$. The resulting radial fiber direction serves to bear the centrifugal load. For the real demonstrator construction, the orientations must be designed in more detail to ensure structural integrity under different operational conditions. A method according to Kleinwechter et al. [24] can be used for this purpose.

In this work, the actuators are applied onto the blade body. However, the objective for the demonstrator manufacturing is to integrate the actuators into the blade body. The integration ensures that the aerodynamic performance of the blade is not negatively affected. To take this into account when analysing feasibility, the dimensions of the actuators are defined in this investigation in a manner that ensures no overlap during future integration. Therefore, the actuators run over the entire span s ($s_s = 0\%$ to $s_e = 100\%$), but run at the chord c only from $c_s = 20\%$ to $c_e = 85\%$. A further expansion in chord-wise direction provokes overlaps at the thin leading and trailing edge regions.

Furthermore, a morphing-related manipulation of the profile cambering is to be investigated by increasing the turning angle $\Delta\varphi$ of the profiles. A definition of the turning angle is

Table 3 Actuator configuration for investigation

Dimensions				Mode	
Spanwise		Chordwise			
s_s	0%	c_s	20%	SS	expansion
s_e	100%	c_e	85%	PS	contraction

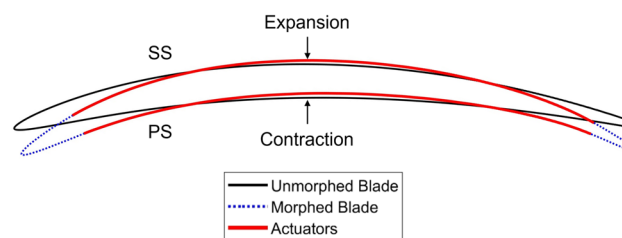


Fig. 9 Principle of turning angle morphing.

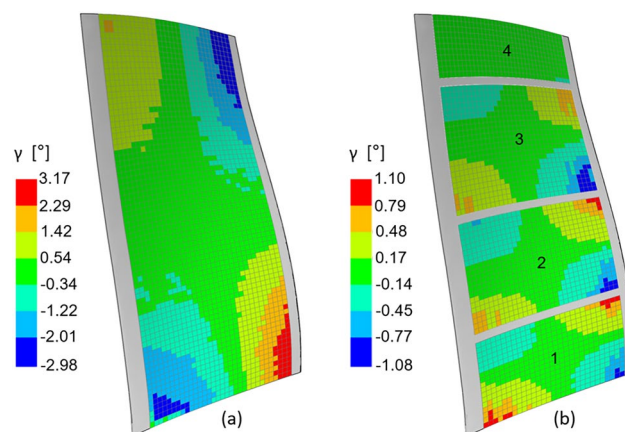


Fig. 10 Shear angle of actuator setup on PS: **a** Continuous actuator, **b** Split actuator array

given in fig. 18 in the appendix. For this purpose, the actuators have an orientation angle of $\theta = 90^\circ$ and therefore run approximately in chord-wise direction. Table 3 summarizes the actuator configuration. Expansion on the SS and contraction on the PS generate an increase in the profile cambering, as illustrated in Fig. 9 and thus a change in the turning angle $\Delta\Delta\varphi$.

Figure 10 (a) shows the draping simulation of the actuators in the configuration from Table 3. Only the pressure side is visualized, as this side provides higher shear angles. The suction side is shown in Fig. 19 in the appendix.

The maximum shear angle of $\gamma = 3.17^\circ$ exceeds the locking angle of $\gamma_{\text{Lock}} = 1.76^\circ$, which suggests that the actuator cannot be applied. Therefore, the actuators must be split in order to reduce the maximum shear angle and enable applicability. For the splitting process, $\gamma_{\text{max}} = 1.17^\circ$ is defined as the permissible shear angle resulting from the experimentally determined locking angle and a chosen safety factor of 1.5.

Figure 10 (b) shows the resulting split actuator array with the individual shear angles on the PS (SS see appendix

Table 4 Spanwise dimensions of split actuator array

Actuator		1		2		3		4	
s_{s1}	0%	s_{s2}	23%	s_{s3}	51%	s_{s4}	84%		
s_{e1}	21%	s_{e2}	49%	s_{e3}	82%	s_{e4}	100%		

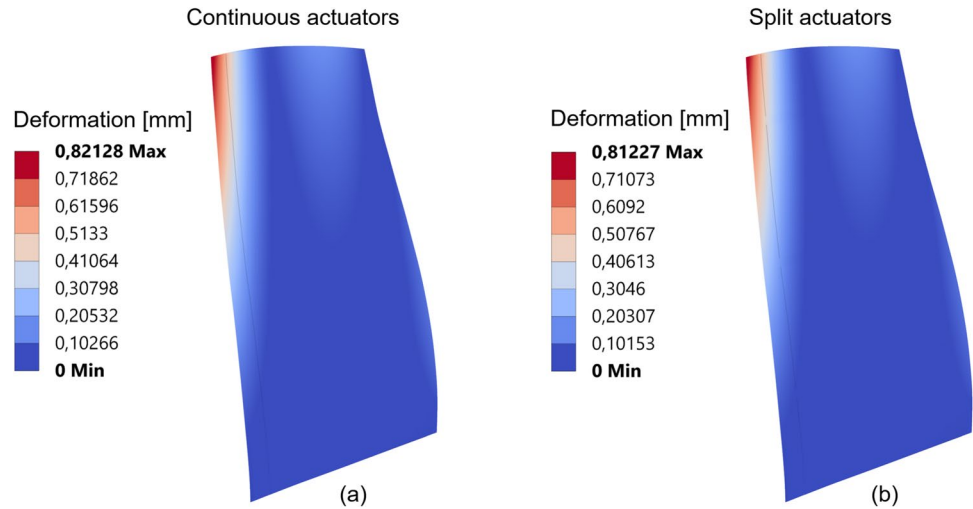
Fig. 11 Morphing deformation of the CFRP fan blade under centrifugal load: **a** Continuous actuators, **b** Spitted actuators

Fig. 12 First actuators of developed array applied onto SE²A fan blade

Fig. 22). The resulting split actuator array on the PS and SS consists of four actuators with individual spanwise start and end positions, which are shown in Table 4.

Due to the splitting, the maximum shear angle in the array is $\gamma = 1.10^\circ$ and thus below γ_{max} , which simulatively confirms applicability. Based on the developed actuator layout, Fig. 11 visualizes the morphing deformation for the continuous and split actuators, which is calculated on the basis of equation (8).

The configuration with continuous actuators enables a maximum morphing deformation of 0.821 mm, while the configuration with the split array achieves a maximum deformation of 0.812 mm.

3.4 Discussion of draping analysis

In Sect. 3.3, the applicability of the developed actuator array was ensured with the Ansys-intern draping algorithm. The utilization of the pin-joined-net model and the associated idealization of the MFC actuators as uncured unidirectional fiber-reinforced composite material represents a significant abstraction. But currently, there are no established methods for predicting the draping behavior of stiffer film-like materials. Consequently, the results of the draping simulation must be critically scrutinized with regard to their physical significance. Furthermore, the investigations are limited to the specific application of the SE²A fan blade, as it was used to determine the locking angle. Nevertheless, Fig. 12 confirms the prediction of the applicability for the actuator 1 on PS and SS.

The application of actuator 2 is shown in appendix (Fig. 20). Actuators 3 and 4 can't be examined in a practical way within this investigation, given that custom actuator shapes were cut from commercially available rectangular MFCs, and actuators with large enough surfaces are not available from the manufacturer. However, the successful application of the first two actuators provide an initial confirmation of the methodology.

Thus, a possibility was created to analyze the feasibility of draping low-profile actuators for morphing engine blades. The approach can be efficiently integrated into the existing design and optimization process from [21, 24] within Ansys without developing a novel methodology for the draping simulation of stiff layered materials. Further

in-depth studies are required to assess the physical correctness of the draping simulation and its applicability to other geometries.

The applicability of the actuators to the scaled SE²A UHBR fan blade is made possible by the split of the continuous actuators, which reduces the active actuator area on the PS/SS and influences the morphing behavior. On the PS the active area is decreased by 6% from 215.86cm² to 202.92cm² and also on the SS by 6% from 220.62cm² to 207.44cm², leading to a combined active area on PS and SS of 410.36cm². Figure 11 shows comparable morphing deformations with a reduction of 1,1% in the maximum deformation.

For a more detailed analysis, the variations of turning angle $\Delta\Delta\varphi$ along the span are considered in Fig. 13. Both configurations demonstrate no change in turning angle at the root, which is a consequence of the fixed support in the FEA. Towards the blade tip, higher turning angle morphing values are achieved, as the blade exhibits reduced stiffness due to the lower profile thickness at the tip. Both configurations show similar graph shapes, with the split actuator configuration producing slightly smaller angular changes, due to the smaller actuator area. The maximum angular change at the tip is $\Delta\Delta\varphi = 1.80^\circ$ with continuous actuators and $\Delta\Delta\varphi = 1.78^\circ$ with a split array, representing a 1.11% decrease in morphing performance at the tip. In general, splitting of the actuators does not result in a significant decline in morphing performance.

3.5 Expected aerodynamic effects

Morphing investigations for the same fan geometry, but with titanium as blade material have shown that a turning angle increment of 0.91 ° at the blade tip leads to an alteration of the rotor's vortex design. With that the loading at the blade tip is increased and higher pressure ratios are achieved. The leading edge metal angle is simultaneously

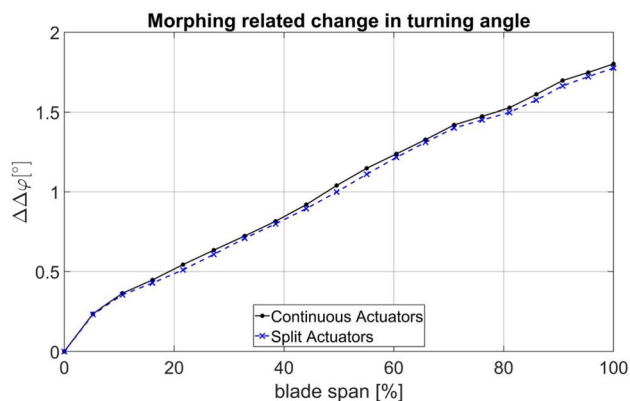


Fig. 13 Change in turning angle caused by continuous and split actuators

increased, which allows to compensate for higher inflow incidence angles. For throttled conditions at design speed as well as part-load operation, the strength of the blade shock interaction is moderate and efficiency benefits up to 0.8 % can be achieved. These results are however depending on the stationary test rig working line and the corresponding intersection points with the fan stage speed lines. Relating the achievable thrust in the electrically test rig set-up to the power required to drive the fan geometry, yields a 0.22 % improvement of the thrust-to-power ratio. Since the increment in tip loading accelerates the positive morphing effects, higher angular morphing values are expected to further accelerate the achievable performance benefits.

3.6 Conclusions on the morphing investigation

Finally, the feasibility of a morphing CFRP fan blade can be confirmed with respect to the applicability of low-profile actuators. In addition, a simplified method for predicting the draping behavior of MFC actuators is available for the SE²A fan blade, which can be used in the demonstrator development. For the final morphing prototype the distances between the active actuator surfaces may have to be increased, since *Kapton* foil is required at the actuator edges (see Fig. 6). Nevertheless, it is also possible to envisage custom actuators connected via compact double-curvature-compensating and energy-conducting areas in one array. This would enable short distances between active piezoelectric areas and one central energy supply for all active areas in an array. In the end, the feasibility of such a concept depends on the final actuator configuration. With the goal to maintain the morphing performance and the positive aerodynamic morphing effects, a minimization of the actuator distances is however recommended.

4 Feasibility of actuators electrical power supply

Based on the findings of the structural design in sect. 3, the feasibility of the developed fan morphing technology can now be analysed at aircraft system level. Therefore, the feasibility of an electric power supply for the piezoelectric actuators is addressed. The actuators applied to each blade, are supplied by the Electric Power System (EPS) of the reference aircraft, initially developed in SE²A [35]. Consequently, the total power consumption of the actuators is estimated, and their integration into the EPS is planned using power interfaces.

For this purpose, the morphing blade structure from sect. 3, which was developed for the test bench application, is scaled up to aircraft-level. To thoroughly assess the



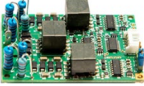
impact of incorporating actuator power demands into the overall system, various power system architectures with different engine configurations, including 2, 4, and 6 motors, are considered. In this paper, the terms 'motor' and 'engine' are used interchangeably, with 'motor' referring to the integrated electrical motor within the system's engine.

4.1 Power supply interface between the EPS and MFCs

Generally, there are two ways to feed the MFC P1 actuators. First, using the commercially available High Voltage power Amplifiers (HVAs) manufactured by Smart Material [27] and alternatively, using a designed power interface, which is modified to match both the main power system and the actuator load profile, as exemplified in [36]. Moreover, there are different topologies for multiport isolated with transformer or non-isolated DC-DC converters documented in the literature, which can be taken into account for this application [37–39].

In this study, the power supply interface is implemented using an existing HVA module, as the focus of this paper does not encompass the design of power electronics. HVAs are designed to be powered by a battery and require a (Direct Current) DC supply voltage from 12 V to 16 V. They can generate DC output voltages from -500 V to 1500 V, which are required to drive the MFCs effectively. Besides, their output is variable and controllable by applying additional control signals. Different control signals are applicable to adjust the HVA's DC output, comprising of an analog signal (0 to 5 V or -2.5 to 7.5 V), a Pulse Width Modulation (PWM), and communication protocols like I²C (Inter-Integrated Circuit). This adjustability enables precise control over the voltage amplitude and rapid switching between different DC voltage levels, allowing for accurate manipulation

Table 5 High voltage power boards for supplying MFCs, manufactured by Smart Material [27].

		
AMD2012-CE2/3 (2011)	AMT2012-CE3 (2015)	MicroHVA-2 (2020)
No. of Channels:		
1	2	2
Input Voltage:		
$8 \sim 15$ Vdc	$8 \sim 15$ Vdc	$12 \sim 16$ Vdc
Input Current:		
114 mA (1.4 W)	230 mA (2.8 W)	2 A ($\approx 12 \times 2$ W)
Output Voltage:		
$-500 \sim 1500$ Vdc		
Bias Port: 500 Vdc (fix), HV Port: 0 \sim 2000 V (variable)		
Operating Temperature:		
$-40 \sim 75$ °C	$-40 \sim 75$ °C	$0 \sim 40$ °C
Input Signals:		
Analog (0 \sim 5 V / PWM (1 \sim 2 ms))		

of the MFCs' deformation and movement. Smart Material suggests different types of HVA modules for harnessing the full potential of MFC P1 actuators. Table 5 presents three of these solutions and their key electrical specifications.

By comparing these options, MicroHVA-2 is selected for further analysis in this work, due to its higher maximum input current and the ability to supply two MFCs through separate channels.

It is important to note that to maintain the required supply voltage for the MFCs within the range of -500 to 1500 V, the only feasible method to increase the number of MFCs is through parallel configuration. Consequently, single-channel and dual-channel types allow for one and two parallel branches, respectively, to connect additional MFCs to the boards. Therefore, the dual-channel board, with its superior maximum input current, is considered the optimal choice. To supply the entire actuator network mounted on all blades, multiple HVAs will be required. The exact number of HVAs needed can be determined by estimating the total power requirements of the actuators, as summarized in the following section.

4.2 Results of power supply

The results of the power supply investigation are split into two steps. First, the power supply sizing to meet MFCs power demand is focused. Then, the proposed MFCs power supply integration into the whole aircraft EPS is discussed through analysis.

4.2.1 Power demand calculations and power supply Sizing

To accurately determine the appropriate power supply board for the total power requirements of the MFCs attached to the aircraft blades, it is necessary to specify the required power concerning a defined MFC surface area in m^2 . Based on the MFC model P1 [27], the poled capacitance of the actuator is approximately 0.3 nF/cm², measured at 1 kHz and room temperature. This indicates that the power required by these voltage-dependent actuators is proportional to the active area of the MFC, so a larger active area results in higher capacitance and consequently greater power demand. Figure 14 illustrates a generally desired voltage waveform for supplying the MFCs for two different scenarios. In the first scenario, actuators on PS and SS are supplied by positive U_p and negative U_n pulse voltages, respectively, as shown in Fig. 14 (a). This configuration allows a quasi-static shape adjustment by manipulating the turning angle for different flight phases, as described in sect. 3. The blade experiences a constant deformation as long as the voltage is applied to each side and the amount of turning angle morphing is controlled by the level of U_p and U_n . It should be noted that the manipulation of the

Fig. 14 Voltage supply waveform scenarios for MFC P1: **a** Turning, **b** Vibration

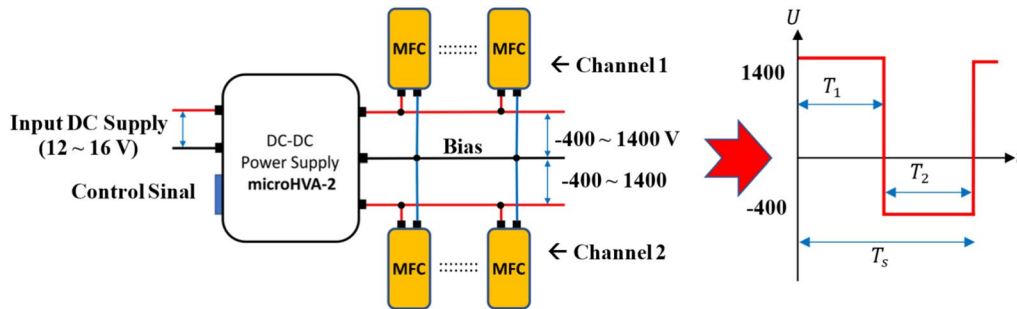
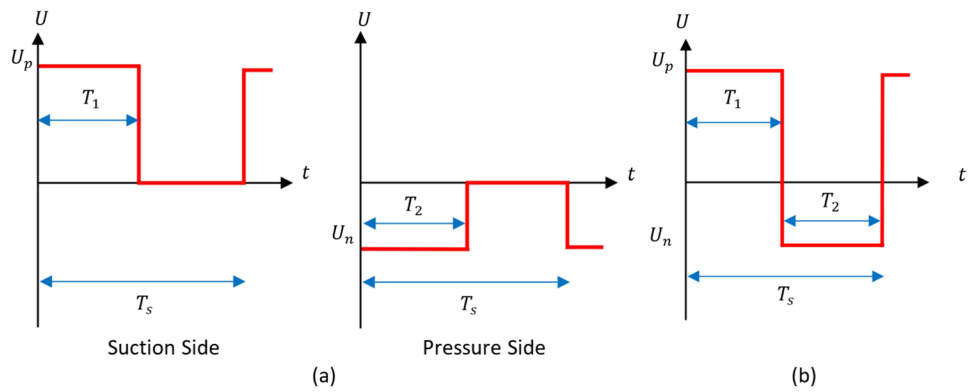


Fig. 15 The DC-DC power board MicroHVA-2 ports arrangement

turning angle is considered an example within this investigation. By varying the actuator fiber orientation and the actuator mode (expansion or contraction) different quasi-static shape changes are feasible, including a manipulation of the blade’s twist. A different actuator configuration however requires an own individually adapted analysis.

In the second scenario, as shown in Fig. 14 (b), the goal is to have a fast actuation movement. This is due to the fact that with high actuation frequencies, the morphing technology would also allow for active vibration control or cyclic periodical adjustments as shown in [8] for future engine applications. Here, it is important to use the full range of motion of the actuators as fast as possible by applying a square wave AC voltage with a higher frequency compared to the first scenario. This is mainly because, in an anti-vibration mode, fast reactions of the MFCs are required. In this study, the first scenario was taken into account for analysis since the quasi-static morphing for different flight phases marks the main focus for the morphing technology development. However, to ensure a practical sizing of the actuator power supply integrated into the EPS and assess its feasibility, the voltage waveform for the vibration scenario is taken into account.

While the waveforms shown in Fig. 14 are alternating waveforms, the used DC to DC power board (MicroHVA-2) can generate this waveform using the control signal. The MicroHVA-2 has three separate ports: One for fixed 500 Vdc and two for channels with a controllable voltage ranging 0

to 2000 Vdc versus the board ground port. This results in a controllable voltage range -500 Vdc to 1500 Vdc for both channels, as depicted in Fig. 15. Within this investigation, the voltage range is limited from -400 Vdc to 1400 Vdc as shown in sect. 3.2.3.

Considering the AC voltage across the inherently capacitive MFC loads, the requested power P_{MFC} can be achieved by

$$P_{MFC} = \frac{U_{RMS}^2}{X_C} \tag{10}$$

where U_{RMS} is the effective voltage of the waveform, and X_C is the AC impedance of the capacitive load MFC. Considering the square shape waveform of voltage shown in Fig. 14, U_{RMS} are calculated by

$$U_{RMS} = \sqrt{\frac{U_p^2 T_1 + U_n^2 T_2}{T_s}} \tag{11}$$

and X_C is estimated through

$$X_C = \frac{1}{2\pi f C} \tag{12}$$

where f is the supplied AC frequency equals $1/T_s$ and C is the capacitance of the MFC in F .

The quasi-static morphing of the blades to achieve the target shape is completed within a few seconds. For instance, the MFC capacitance charges within 10 s, which is sufficient for slow shape adaption for different flight phases, then it corresponds to a frequency of 0.1 Hz for the turning scenario. In contrast, for the anti-vibration mode, the morphing procedure is performed much faster to act against vibrations induced by the rotational frequency. For an initial estimate, a frequency of 100 Hz is chosen. This is because modern UHBR engine fan blades rotate at approximately 2000 to 4000 rpm [40] or 33.3 to 66.6 Hz. The frequency results in a charging time of approximately 10 ms. Additionally, the high frequency is beneficial in case of fault occurrence in the actuators. In such conditions, the fault clearance control system attempts to promptly restore the power supply, leading to the MFC being charged in a very short time. Consequently, both low and high-frequency scenarios are considered in the actuator power calculations presented in this study.

The total required power of the actuators P_{tot} as well as the number of MicroHVA-2 required N_{HVA} , their volume V_{tot} and weight M_{tot} can be derived using the following calculation procedure:

- **One MFC actuator power demand:**

The MFC power for one unit with a capacitance of 1 nF ($P_{1\text{nF}}$) can be obtained using two independent approaches. Later, the highest calculated value is considered to ensure the supplied power's adequacy.

- **Using equation (10):** $P_{1\text{nF}}$ is calculated for 0.1 Hz and 100 Hz. Considering the voltage operating range ($[-400 \text{ V}, 1400 \text{ V}]$) and assuming $T1 = T2$, U_{RMS} is calculated 1030 V, using the equation (10). In addition, X_C is obtained 1590 M Ω for 0.1 Hz and 1.59 M Ω for 100 Hz, using equation (11). Therefore, using equation (12), $P_{1\text{nF}}$ is determined 0.68 mW and 0.68 W for 0.1 Hz and 100 Hz, respectively.
- **Using capacitor charging time:** According to the MFC's datasheet [27], the charging time from -500 V to 1500 V for an MFC P1 with 5 nF capacitance is less than 10 ms corresponding to 100 Hz. This step-up voltage requires approximately 4 W of power, which must be supplied by the power supply board. Therefore, an MFC P1 with 1 nF capacitance would require 0.8 W/nF (4 W/5 nF) of power.

- **All MFCs total capacitance C_{tot}**

The total capacitance of all MFCs used in the aircraft can be obtained by multiplying the poled capacitance of the MFC P1, $0.3\text{nF}/\text{cm}^2$, with the total active area in the entire propulsion system A_{tot} . To obtain A_{tot} , the

active area of each blade A_{bld} is derived using the aerodynamic scaling procedure for different motor number scenarios, explained in sect. 4.2.2. By multiplying the active area per blade with the number of blades N_{bld} in each fan section, the active area per fan A_{fan} is calculated. By multiplying the number of motors N_{motor} with the area per fan, the active area for the entire system A_{tot} is derived.

- **All MFCs total power demand P_{tot}**

P_{tot} can be determined by scaling the power consumption of the 1 nF capacitor, $P_{1\text{nF}}$, proportionally to the increase in capacitance. To this end, the total power required to supply the actuators is calculated by multiplying the power-to-capacitance ratio of one MFC unit (obtained as 0.8 W/nF) with total MFCs capacitance C_{tot} .

- **Total number of required MicroHVA-2 boards N_{HVA}**

As explained earlier, since MFC integration into passenger aircraft engine blades has not yet been commercialized, the physical characteristics of a special DC-DC power supply can be implemented using the MicroHVA-2. Thus, N_{HVA} can be determined through two methods: 1- dividing total MFCs capacitance C_{tot} by maximum allowable load capacitance of one MicroHVA-2 $C_{\text{MFC, max}}$, denotes as $N_{\text{HVA},1}$, and 2- dividing the total actuator required power P_{tot} by the maximum power of one MicroHVA-2 board $P_{\text{HVA, max}}$, denotes as $N_{\text{HVA},2}$. Table 6 summarizes the MicroHVA-2 specifications and detailed results of the proposed electric supply system for the total installed actuators. As shown in this table, $N_{\text{HVA},1}$ and $N_{\text{HVA},2}$ are close to each other for all motor number configuration scenarios.

- **Total volume V_{tot} and weight M_{tot} of designed power supply**

Finally, V_{tot} and M_{tot} of the designed power supply using MicroHVA-2 boards can be derived by multiplying the volume V_{HVA} and weight M_{HVA} of each MicroHVA-2 board with the total number of the required MicroHVA-2 board N_{HVA} , respectively. Moreover, a casing margin of 1.3 is included to account for the increased volume and weight of the power supply boards when placed in a container. As tabulated in Table 6, all the detailed specifications of the proposed electric supply system are shown for P_{tot} as 6.5 kW, 9.2 kW, and 11.3 kW for 2, 4, and 6 engines, respectively.

4.2.2 Aerodynamic scaling procedure

As the chosen turbofan was originally designed for a potential integration into the Propulsion Test Facility (PTF) of the Institute of Jet Propulsion and Turbomachinery, the engine scaling procedure is based on the test rig power

Table 6 Summarized result of the proposed actuators electric power supply

MicroHVA-2 specifications					
Parameter	Unit	Symbol	Value		
MicroHVA-2 dimension (W x D x H)	mm	-	45 × 67 × 18		
MicroHVA-2 volume	cm ³	V_{HVA}	54.27		
MicroHVA-2 weight	g	M_{HVA}	50		
Maximum input power of MicroHVA-2	W	$P_{HVA, \max}$	24		
Calculated power for 1 nF MFC	W/nF	P_{1nF}	0.8		
Max. allowable capacitance of load ($P_{HVA, \max}/P_{1nF}$)	nF	$C_{MFC, \max}$	30		
Actuators power supply specifications					
Parameter	Unit	Symbol	Number of electric motors (N_{motor})		
			2	4	6
Actuator area per blade (cm ²)	cm ²	A_{bld}	710.76	502.59	410.36
No. of blades	-	N_{bld}	19	19	19
Active area per fan ($A_{bld} \times N_{bld}$)	cm ²	A_{fan}	13504.44	9549.21	7796.84
Active area for the entire system ($A_{fan} \times N_{motor}$)	cm ²	A_{tot}	27008.88	38196.84	46781.04
Total capacitance of all MFCs ($A_{tot} \times 0.3$ nF/cm ²)	nF	C_{tot}	8102.66	11459.05	14034.31
Total power of power supply ($C_{tot} \times P_{1nF}$)	kW	P_{tot}	6.482 ≈ 6.5	9.167 ≈ 9.2	11.227 ≈ 11.3
MicroHVA-2 quantities using $C_{tot}/C_{MFC, \max}$	-	$N_{HVA,1}$	≈271	≈381	≈468
MicroHVA-2 quantities using $1000 \times P_{tot}/P_{HVA, \max}$	-	$N_{HVA,2}$	≈271	≈384	≈471
Total volume of the MicroHVA-2 board ($N_{HVA,2} \times V_{HVA} \times 1.3$)	m ³	V_{tot}	0.0191193	0.0270916	0.0332295
Total weight of the MicroHVA-2 board ($N_{HVA,2} \times M_{HVA} \times 1.3$)	kg	M_{tot}	17.6	24.9	30.6

requirements as well as the original main dimensions of the test rig rotor design [25, 41]. The major output of the scaling procedure is the blade suction and pressure side surface in order to determine the electric power supply requirements for the actuators. In addition to an upscaling of the original fan design for a conventional twin-engine aircraft architecture (Sect. 4.2.3), different distributed propulsion concepts are considered within this investigation due to its performance enhancement potential [42].

Since it is not possible to maintain a perfect fluid mechanics and geometry similarity when scaling [9], this straightforward aerodynamic scaling method supports the preliminary design phase and is only based on Mach number and geometry similarity. The Reynolds number and its effect on the boundary layers can not simultaneously be maintained, as well as the blockage effects of the scaled fan stage are neglected.

Investigating an electrical powerplant design, the engine core, fuel mass flow rate and bleed air mass flow rate are nonexistent compared to conventional propulsion systems, which results in an infinite bypass ratio and constant mass flow rate. Due to higher mass flow rates than 70 kg/s, the polytropic efficiency is considered to be not affected by upscaling [43]. Furthermore, the nozzle efficiency and the nozzle exit velocity are presupposed to be constant for the same flight conditions.

Starting with the test rig fan design, the propulsion power P_{pr} is derived from the demand of electrical power P_{el} at the design point considering the propulsive efficiency η_{pr} :

$$P_{pr} = \underbrace{\dot{m}(v_{in} - v_{out})}_{\text{constant}} v_f = \eta_{pr} P_{el} \quad (13)$$

With the simplified boundary conditions the propulsion power only depends on the mass flow rate \dot{m} , which is proportional to the square radius of the circular cross-sectional area of the engine. As the radius is proportional to the blade height and therefore to the actuator area, the scaled area can be derived from the electric power ratio:

$$A_{act, \text{scaled}} = A_{act, \text{design}} \sqrt{\frac{P_{el, \text{scaled}}}{P_{el, \text{design}}}} \quad (14)$$

The required electrical power supply for the actuators can be derived from the scaled actuator area for the respective aircraft architecture.

4.2.3 Power supply integration into the aircraft Electric Power System (EPS)

As a part of the SE²A, three energy-efficient aircraft have been designed to accommodate the majority of commercial

aircraft operations: Short-range, medium-range, and long-range [35]. In this study, the medium-range reference aircraft is considered, which has mission requirements comparable to an Airbus A320 and initially has a design range of 4600 km for maximum payload and cruise altitude of 8000 m. In order to have a rough estimation of the reference aircraft's total demanded power by shaft, a typical mission profile for this aircraft is assumed in SE²A as depicted in Fig. 16.

The maximum shaft power P_{shaft} usually occurs in the take-off phase, based on a basic relation with the thrust Th_{shaft} , velocity v , propulsive efficiency η_{pr} , and throttle Tr setting. P_{shaft} is considered as the total shaft power for a fully electric powertrain aircraft, calculated as follows using the procedure explained in [44].

$$P_{\text{shaft}} = \frac{Th_{\text{shaft}} v}{\eta_{\text{pr}} Tr} \quad (15)$$

Where Th_{shaft} is considered 58.56 kN, v is set to 117.98 m/s, η_{pr} is assumed to be 0.9, and Tr is considered 0.656, resulting in 11.702 MW, which is rounded to 12 MW.

Following the trajectory towards the electrification of conventional aircrafts, future partially or fully electrified aircraft will incorporate an on-board EPS. The generic EPS structure of a conceptual fully electrified aircraft with four propulsors is shown in Fig. 17. As observed in this figure, the EPS is distributed over a main high-voltage DC busbar. The Electrochemical Energy Storages (EESs) including batteries and/or fuel cells are connected to the busbar through DC-DC converters and power cables (gray lines). In the middle, there is an electric panel equipped with circuit breakers to protect and distribute the required

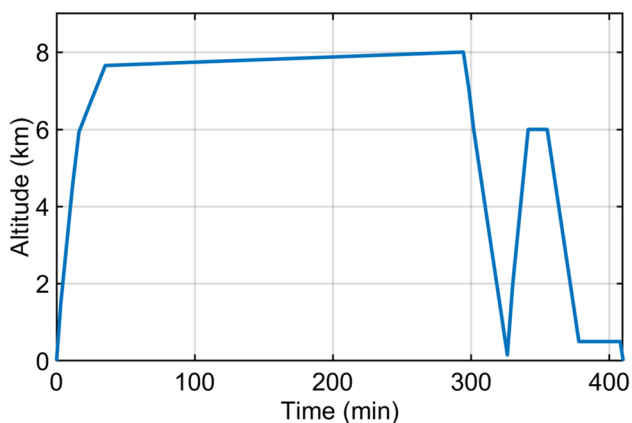


Fig. 16 Typical mission profile commissioned in SE²A for mid-range future concept aircraft.

power through power cables to DC-AC inverters, followed by electric motors. Nevertheless, this fully electric medium-range aircraft design is only possible with huge advancements in EESs as well as reaching high power dense electric components. Therefore, an innovative high-power dense modular electric motor with an embedded inverter described in [45] is utilized for the EPS design. This electric motor has a specific power and power density of 12 kW/kg and 17.25 MW/m³, respectively, with a minimum power of 1.5 MW and a maximum of 6 MW, thanks to modularity features.

As stated previously, it is preferred that the power required for the MFCs is provided through a standalone DC-DC power supply with a special design for this application. This power supply converts a fixed medium-level DC grid voltage on the DC busbar to the desired DC voltage demanded by the integrated MFC actuators. As shown in Fig. 17, two standalone devices of this special DC-DC power supply called “MFC Conv. 1 and 2” are considered. The converters can be located near the engines and the power can be transmitted with separate MFC cables (green and red lines) to the MFCs on the blades. As visualized, each converter can individually supply the MFCs on all engines, contributing to higher redundancy and reliable operation in case of a fault happening on one side of the EPS. Furthermore, since the blades on the engine's fan are turning, slip rings on the fan bearings are the solution to transfer power to the blades.

4.3 Discussion of power supply

The justification of integrating MFCs into the engine blades in future fully electrified / hybrid aircraft is better realized by comparing the total power consumption of high-frequency MFCs (6.5 kW, 9.2 kW, and 11.3 kW) with the maximum total 12 MW shaft power in the reference passenger aircraft. Since the MFC power supply is less than 0.1 % of the propulsion system power, integration into the electric power system is no concern. In the context of quasi-static and slow morphing, the aforementioned statement is further reinforced, since lower actuation frequencies lead to lower power requirements.

As shown in Fig. 17, two separate DC-DC converters were considered in an electric aircraft for feeding the MFCs on all blades. But it is worth mentioning that even in conventional combustion aircrafts, MFC integration would be possible by supplying the MFCs power with an Auxiliary Power Unit (APU) alongside a small backup battery bank.

In addition, the MFC integration is further justified when comparing the physical characteristics of the proposed EPS

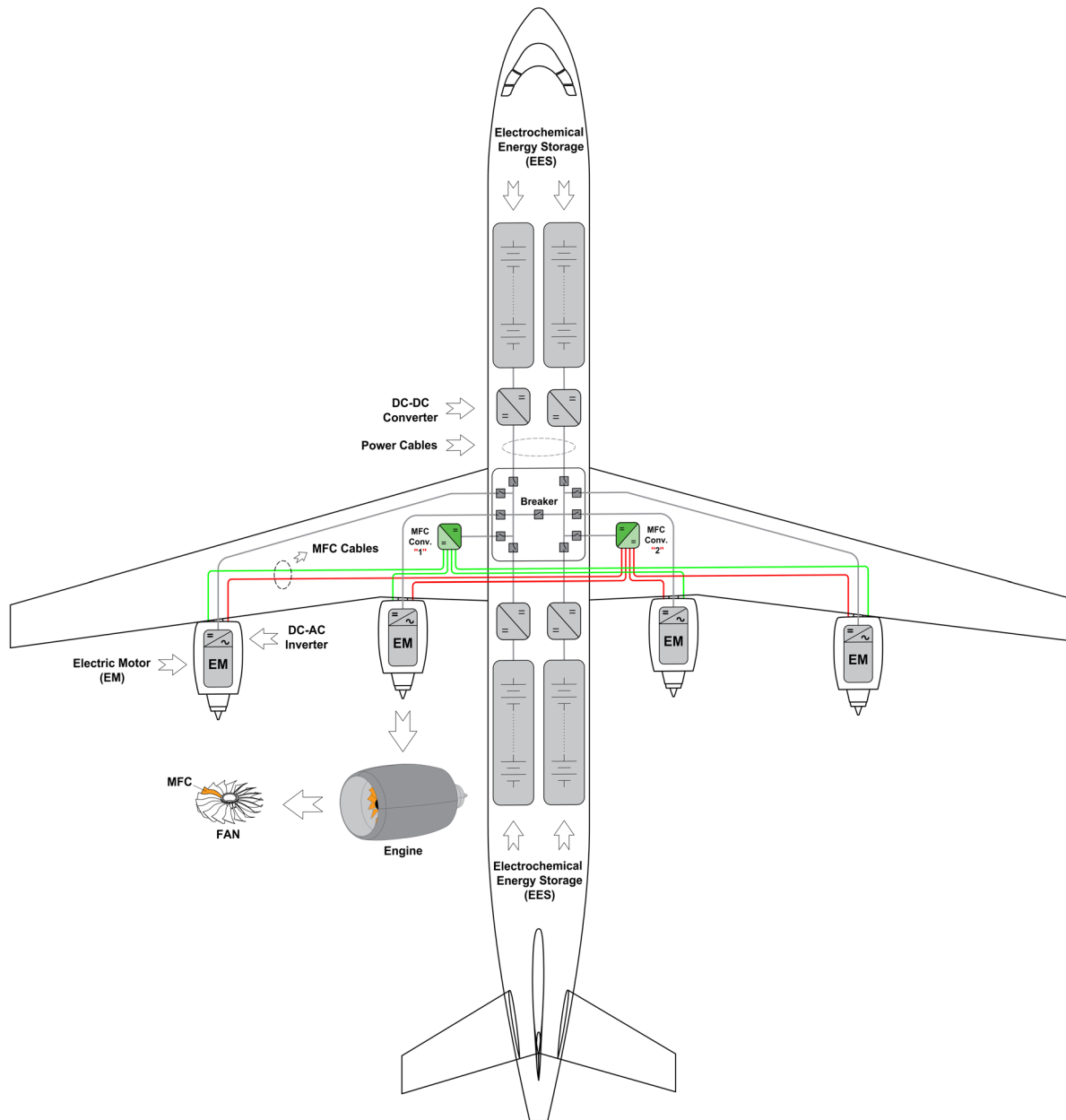


Fig. 17 Special MFCs’ DC-DC converter integration into the aircraft electric power system

Table 7 Aircraft EPS performance characteristics.

No. of motors (N_{motor})	Power (kW)	Weight (kg)	Volume (m^3)	Specific power (kW/kg)	Power density (MW/m^3)
2	12000	1821	1.197479	6.58	10.02
4	12000	1869	1.217896	6.42	9.85
6	12000	1891	1.227904	6.34	9.77

for the fully electrified reference aircraft. Table 7 summarizes the key performance characteristics, including power, weight, volume, specific power, and power density for the

EPS of the medium-range reference aircraft, evaluated for the configurations with 2, 4, and 6 motors.

The proposed EPSs for all three configurations are sized by using the specific power and power density values of 22KW/kg and $37.5\text{MW}/m^3$ for DC-DC converters and 12KW/kg and $17.25\text{MW}/m^3$ for electric motors with embedded inverters. The weights and volumes (excluding electrochemical energy storages) of the EPSs are estimated as 1821kg , 1869kg , and 1891kg and 1.19m^3 , 1.21m^3 , and 1.22m^3 for 2, 4, and 6 motor configurations, respectively. Whereas based on Table 6, the calculated weight and

volume values of the MFCs power supply for corresponding motor configurations are 17.6kg, 24.9kg, 30.6kg and 0.0191193m³, 0.0270916m³, 0.0332295m³, respectively. Comparing these values, the weight and volume of the MFC power supply are at least 62 and 36 times lower than those of the EPS, respectively.

5 Summary and outlook

This paper examines the feasibility of shape-variable engine blading with piezoelectric low-profile actuators by conducting a sequential multidisciplinary analysis from component-level up to aircraft-system-level. The analysis commences with the aerodynamic design of the blade geometry, which follows current UHBR design trends. Even at this early stage, the morphing technology is also taken into account by increasing the deformability through the implementation of a high aspect ratio and a forward sweep.

Based on the developed geometry, the CFRP structure of the blade including the piezoelectric MFC actuators can be analyzed. The focus is the drapability of the actuators onto the strongly double-curved surfaces of the blade, a crucial aspect for the viability of the morphing concept. By abstracting the actuators as an unidirectional textile, a commercial draping algorithm with a strain energy minimization approach could be applied. Splitting of the continuous actuators based on an experimentally determined locking angle resulted in actuator arrays with simulated shear angles below the locking angle. This simulated prediction of drapability was also confirmed experimentally for two actuators. By using a structural model consisting of 42 layers of M21 E prepreg and applied MFC actuators, the morphing deformation can be simulated with a FEA. The reduction in active actuator area resulting from the necessary splitting led to a reduction in the achievable morphing related change in turning angle by 1.11 % to 1.78 °. Therefore, the draping of piezoelectric low-profile actuators is considered feasible when employing the split approach.

Finally, the findings from the development of the morphing fan blade's structure enable the feasibility analysis of the morphing technology at aircraft-system-level. Therefore, the blade developed for test bench use is scaled up and the integration into the EPS of a future electric aircraft is addressed. As the MFC actuators permit high actuation frequencies, which can be utilized for cyclic periodic actuation or vibration reduction, a high frequency is included into the analysis. Considering three different power system architectures with various numbers of engine configurations, including 2, 4, and 6 motors, a high-voltage power

supply for the actuators was designed by 271, 384, and 471 high-voltage power boards. In this regard, the required power for an actuation frequency of 100 Hz, considering all motor configurations (6.5 kW, 9.2 kW, and 11.3 kW), can be easily integrated into the aircraft's 12 MW electrical power system.

Based on the findings of the holistic feasibility analysis, the design and construction of technology demonstrators at test-bench-level can commence. For this purpose, the blade's structural design must be finalized including the integration of the MFC actuators into the CFRP laminate. For the subsequent possible technology transfer to full-scale aircraft-level, further work must be carried out on the electrical power supply system. This work may focus on a novel power electronics design tailored to the MFC P1 actuators, developing a custom power interface and exploring various multi-port DC-DC converter topologies to match the system's optimal performance. Furthermore, future work could explore methods for transferring power from the stationary DC-DC power supply to the actuators installed on the rotating blades.

Appendix

See figures (18,19 and 20)

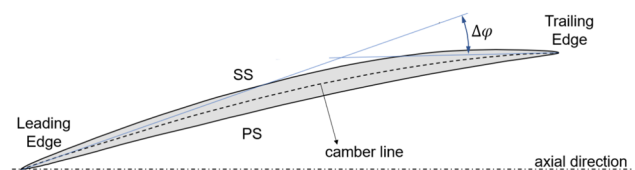


Fig. 18 Definition of turning angle $\Delta\varphi$ on aerodynamic profile



Fig. 19 Shear angle of actuator setup on SS: **a** Continuous actuator, **b** splitted actuator array

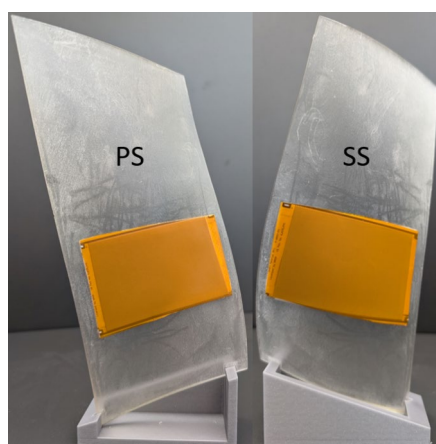


Fig. 20 Second actuators of array

Acknowledgements We would like to acknowledge the funding by the Deutsche Forschungsgemeinschaft (DFG, German Research Foundation) under Germany's Excellence Strategy – EXC 2163/1- Sustainable and Energy Efficient Aviation – ProjectID 390881007.

Author Contributions F.K. and H.M. were responsible for the draping analysis of the piezoelectric actuators and FEA of the morphing related deformation. A.N., A.M. and M.T. were responsible for the analysis of an electrical power supply system for the piezoelectric actuators. T.R., M.S. and J.F. were responsible for the fan blade geometry and aerodynamic scaling. All authors reviewed the manuscript.

Funding Open Access funding enabled and organized by Projekt DEAL. This work was funded by the Deutsche Forschungsgemeinschaft (DFG, German Research Foundation) under Germany's Excellence Strategy – EXC 2163/1- Sustainable and Energy Efficient Aviation – ProjectID 390881007.

Data availability Data can be made available from the authors upon reasonable request.

Code availability Code regarding the analysis of draping, aerodynamic scaling and sizing of electric power supply can be made available from the authors upon reasonable request.

Declarations

Conflict of interest The authors declare no competing interests.

Ethics approval and consent to participate not applicable due to lack of guidelines.

Consent for publication not applicable due to lack of guidelines.

Competing interests The authors declare no competing interests.

Open Access This article is licensed under a Creative Commons Attribution 4.0 International License, which permits use, sharing, adaptation, distribution and reproduction in any medium or format, as long as you give appropriate credit to the original author(s) and the source, provide a link to the Creative Commons licence, and indicate if changes were made. The images or other third party material in this article are included in the article's Creative Commons licence, unless indicated otherwise in a credit line to the material. If material is not

included in the article's Creative Commons licence and your intended use is not permitted by statutory regulation or exceeds the permitted use, you will need to obtain permission directly from the copyright holder. To view a copy of this licence, visit <http://creativecommons.org/licenses/by/4.0/>.

References

- Barbosa, C.F.: Ultra High Bypass Ratio Engine Technology Review - The Efficiency Frontier for the Turbofan Propulsion. In: SAE Technical Paper Series 2021, Virtual, Online (2021). <https://doi.org/10.4271/2021-36-0032>. SAE BRASIL 2021 Web Forum
- Wei, J., Zhang, Y., Liu, Y., Wang, Y., Li, C., Sun, Z., Xu, H., Shao, H., Zhang, D., Zou, Q., Zhang, Q., Feng, J., Kong, W., Jiao, Y., Chen, L.: Advances in resin matrix composite fan blades for aircraft engines: A review. *Thin-Walled Structures* **202**, 1112058 (2024). <https://doi.org/10.1016/j.tws.2024.112058>
- Benini, E., Mistry, C., Wadia, A.R.: Historical Developments in Fan Technologies for Aeroengines. In: Turbo Expo: Power for Land, Sea and Air, Volume 13A, Boston, USA (2023). <https://doi.org/10.1115/GT2023-101639>. ASME Turbo Expo 2023
- General Electric (GE) Aerospace: GE9X Engine. <https://www.geaerospace.com/commercial/aircraft-engines/ge9x>. (Accessed 16 January 2025)
- CFM International: RISE. <https://www.cfmaeroengines.com/rise/>. (Accessed 16 January 2025)
- Kavvalos, M.D., Kyprianidis, K.G., Padulo, M.: The growth engine concept and its potential for an electrified aviation future. *J. of Engineering for Gas Turbines and Power* **146**, 070901 (2024). <https://doi.org/10.1115/1.4063193>
- Cumpsty, N.A.: *Jet Propulsion*. Cambridge University Press, Cambridge (2011)
- Seidler, M., Voigt, J., Montano Rejas, Z.M., Friedrichs, J., Riemenschneider, J., Monner, H.P.: Aerostructural investigation of shape adaptive rotor blading for the reduction of BLI induced losses in the distorted flow regimes of a transonic fan rotor. In: ECCOMAS PROCEEDIA, Patras, Greece (2023). <https://doi.org/10.7712/150123.9790.444574>. ECCOMAS SMART Conference 2023
- Joos, F.: *Aerodynamik Axialer Turbokompressoren*. Springer, Wiesbaden (2020)
- Mazzawy, R.S.: Performance Study for the Benefits of a Variable Pitch Composite Fan. In: Turbo Expo: Power for Land, Sea and Air, Volume 1, Glasgow, UK (2010). <https://doi.org/10.1115/GT2010-22148>. ASME Turbo Expo 2010
- Mennicken, M., Arzberger, M.J., Schnell, R.: Exploring the Operational Strategy of an Electrically-Driven Variable Pitch BLI-Fan, Ottawa, Canada (2022). ISABE Conference
- Moreau, A., Schnell, R., Mennicken, M.: Acoustic preliminary design of a low-noise fan stage considering a variable-area nozzle and variable-pitch rotor blades. *CEAS Aeronautical J.* **14**, 325–341 (2023). <https://doi.org/10.1007/s13272-023-00658-x>
- Wall, B.G., Lim, J.W., Riemenschneider, J., Kalow, S., Wilke, G.A., Boyd, D.D., Jr., Bailly, J., Delrieux, J., Cafarelli, I., Tanabe, Y., Sugawara, H., Jung, S.N., Hong, S.H., Kim, D.H., Kang, H.J., Barakos, G., Steininger, R.: New smart twisting active rotor (star): Pre-test predictions. *CEAS Aeronautical J.* **15**, 721–750 (2024). <https://doi.org/10.1007/s13272-024-00731-z>
- Kalow, S., Keimer, R., Kamp, B., Riemenschneider, J.: Next generation active twist helicopter rotor blade - simulated results validated by experimental investigation, Warsaw, Poland (2019). 45th European Rotorcraft Forum
- Fortini, A., Suman, A., Aldi, N., Merlin, M., Pinelli, M.: A shape memory alloy-based morphing axial fan blade-part I: Blade

- structure design and functional characterizations. *J. of Engineering for Gas Turbines and Power* 138, 022601 (2016) <https://doi.org/10.1115/1.4031272>
16. Suman, A., Fortini, A., Aldi, N., Merlin, M., Pinelli, M.: A Shape Memory Alloy-Based Morphing Axial Fan Blade: Part II - Blade Shape and CFD Analyses. In: *Turbo Expo: Power for Land, Sea and Air*, Volume 5, Montreal, Canada (2015). <https://doi.org/10.1115/GT2015-42700>. ASME Turbo Expo 2015
 17. Krone, J.H., Huxdorf, O., Riemenschneider, J., Monner, H.P., Schur, F., Friedrichs, J., Wiedemann, M.: Experimental investigation and design of a shapevariable compressor cascade. *CEAS Aeronautical J.* 8, 105–127 (2017) 0.1007/s13272-016-0224-1
 18. Li, C., Pan, T., Yan, Z., Zheng, M., Li, Q., Dowell, H.: Aerodynamic characteristics of morphing supersonic cascade under low-upstream-mach-number condition. *AIAA J.* 61, 1708–1719 (2023). <https://doi.org/10.2514/1.J062563>
 19. Abate, G., Riemenschneider, J.: Multi-disciplinary and multi-objective optimization problem applied to a morphing blade cascade study. *J. of Intelligent Material Systems and Structures.* 36, 119–128 (2024) <https://doi.org/10.1177/1045389X241294104>
 20. Tweedt, D.L.: Preliminary Aerodynamic Investigation of Fan Rotor Blade Morphing, Cleveland, Ohio, USA (2012). NASA Glenn Research Center
 21. Montano Rejas, Z.M., Seidler, M., Riemenschneider, J., Friedrichs, J.: A coupling method for the design of shape-adaptive compressor blades. *Appl. Mechanics* 3, 182–209 (2022). <https://doi.org/10.3390/applmech3010014>
 22. Montano Rejas, Z.M., Seidler, M., Riemenschneider, J., Friedrichs, J.: Aerodynamic validation for compressor blades' structural morphing concepts. *CEAS Aeronautical J.* 14, 139–154 (2023). <https://doi.org/10.1007/s13272-022-00624-z>
 23. Seidler, M., Montano Rejas, Z.M., Friedrichs, J., Riemenschneider, J.: Introduction and evaluation of an aerostructural coupling approach for the design of shape adaptive compressor blading, Ottawa, Canada (2022). International Society of Air Breathing Engines (ISABE) Commfernece
 24. Kleinwechter, F., Seidler, M., Monner, H.P., Friedrichs, J.: Structural Design and Optimization of Piezo-Activated Morphing CFRP Fan Blades. In: *Smart Materials, Adaptive Structures and Intelligent Systems*, Atlanta, USA (2024). <https://doi.org/10.1115/SMASIS2024-139802>. ASME SMASIS Conference
 25. Seidler, M., Bode, C., Friedrichs, J.: Effect of blade reference design variations on the morphing capability of a shape-adaptive fan rotor. *Int. J. of Gas Turbine, Propulsion and Power Systems* 15(2), 60–67 (2024) https://doi.org/10.38036/jgpp.15.2_60
 26. Wilkie, W.K., Bryant, R.G., High, J.W., Fox, R.L., Hellbaum, R.F., Jalink, A., Little, B.D., Mirick, P.H.: Low-cost piezocomposite actuator for structural control applications. In: *Jacobs, J.H. (ed.) Smart Structures and Materials 2000: Industrial and Commercial Applications of Smart Structures*, pp. 323–334. SPIE Proceedings, Newport Beach (2000). <https://doi.org/10.1117/12.388175>
 27. Smart Material Corp.: Smart Material – Home of the MFC. <https://www.smart-material.com/MFC-productmainV2.html>. (Accessed 16 January 2025)
 28. Schmidt-Eisenlohr, C., Voggenreiter, H., Kupke, M.: Experimental method to determine the draping behavior of auxiliary materials for the vacuum bagging of cfpr parts on doubled-curved surfaces. *Appl. Composite Materials* 31, 1219–1235 (2024) <https://doi.org/10.1007/s10443-024-10229-w>
 29. ANSYS Inc.: ACP User's Guide. https://ansyshelp.ansys.com/aaccount/secured?returnurl=/Views/Secured/corp/v241/en/acp_ug/acp_ug.html. (Accessed 16 January 2025)
 30. Wang, J., Paton, R., Page, J.R.: The draping of woven fabric preforms and prepregs for production of polymer composite components. *Composites Part A* 30, 757–765 (1999) [https://doi.org/10.1016/S1359-835X\(98\)00187-0](https://doi.org/10.1016/S1359-835X(98)00187-0)
 31. DuPont: DuPontTM KaptonR Summary of Properties. https://www.dupont.com/content/dam/dupont/amer/us/en/ei-transformation/public/documents/en/EI-10142_Kapton-Summary-of-Properties.pdf. (Accessed 16 January 2025)
 32. Sancak, E., Schmidt-Eisenlohr, C.: Ermittlung von Drapierkennwerten der Vakuumaufbau-Hilfsstoffe für CFK-Strukturen mit doppelt gekrümmten Oberflächen. Master's thesis, Technische Hochschule Ingolstadt, Ingolstadt (2017)
 33. Williams, R.B., Inman, D.J., Schultz, M.R., Hyer, M.W., Wilkie, W.K.: Nonlinear tensile and shear behavior of macro fiber composite actuators. *J. of Composite Materials* 38, 855–869 (2004). <https://doi.org/10.1177/0021998304040555>
 34. Monner, H.P., Huxdorf, O., Riemenschneider, J., Keimer, R.: Design and manufacturing of morphing fan blades for experimental investigations in a cascaded wind tunnel, Kissimmee, USA (2015). <https://doi.org/10.2514/6.2015-0790>. (23rd AIAA/AHS Adaptive Structures Conference)
 35. Karpuk, S., Elham, A.: Influence of novel airframe technologies on the feasibility of fully-electric regional aviation. *Aerospace* 8, 163 (2021). <https://doi.org/10.3390/aerospace8060163>
 36. Debiasi, M., Chan, W., Bouremel, Y., Yap, C.Y.: Shaping of UAV Wings by Macro-Fiber-Composite Actuators. (2013)
 37. Zhang, H., Hanwen, W., Wang, Y., Chen, Z.: Topologies of Isolated Multiport Converters for DC Grid Applications: A Review, Kiel, Germany (2022). <https://doi.org/10.1109/PEDG54999.2022.9923261>. (IEEE 13th International Symposium on Power Electronics for Distributed Generation Systems (PEDG))
 38. Babaei, E., Abbasi, O., Sakhavati, S.: An overview of different topologies of multi-port dc/dc converters for dc renewable energy source applications, Chiang Mai, Thailand (2016). <https://doi.org/10.1109/ECTICon.2016.7561420>. 3th International Conference on Electrical Engineering/Electronics, Computer, Telecommunications and Information Technology (ECTI-CON)
 39. Kanaparthi, R.K., Singh, J.P., Ballal, M.S.: A Review on Multi-Port Bidirectional Isolated and Non-Isolated DC-DC Converters for Renewable Applications, Jaipur, India (2022). <https://doi.org/10.1109/PEDES56012.2022.10080049>. IEEE International Conference on Power Electronics, Drives and Energy Systems (PEDES),
 40. Pagès, V., Duquesne, P., Aubert, S., Blanc, L., Ferrand, P., Ottavy, X., Brandstetter, C.: Uhbr open-testcase fan ecl5/catana. *Int. J. of Turbomachinery, Propulsion and Power* 7, 17 (2022) <https://doi.org/10.3390/ijtp7020017>
 41. Grubert, J., Brunow, P., Friedrichs, J., Lionel, M., Schnell, R., Winkelmann, P., Ortmanns, J.: Design and development of a combined intake fan test rig to enable investigations of stable operating ranges, Ottawa, Canada (2022). International Society of Air Breathing Engines (ISABE) Commfernece
 42. Burston, M., Ranasinghe, K., Gardi, A., Parezanović, V., Ajaj, R., Sabatini, R.: Design principles and digital control of advanced distributed propulsion systems. *Energy* 241, 122788 (2022). <https://doi.org/10.1016/j.energy.2021.122788>
 43. Grieb, H.: Projektierung Von Turboflugtriebwerken. Birkhäuser Verlag, Basel (2004). <https://doi.org/10.1007/978-3-0348-7938-5>
 44. Ebersberger, J., Fauth, L., Keuter, R., Cao, Y., Freund, Y., Hanke-Rauschenbach, R., Ponick, B., Mertens, A., Friebe, J.: Power distribution and propulsion system for an all-electric short-range commuter aircraft-a case study. *IEEE Access* 10, 114514–114539 (2022)
 45. H3X Technologies: HPDM-1500. <https://www.h3x.tech/products/hpdm-1500>. (Accessed 06 February 2025)